Li *et al. Earth, Planets and Space* (2023) 75:59
https://doi.org/10.1186/s40623-023-01813-8

Earth, Planets and Space

FULL PAPER

Longitudinal structures of zonal wind in the thermosphere by the ICON/MIGHTI and the main wave sources

Dan Li[1,2], Hong Gao[1,3*], Jiyao Xu[1,3*], Yajun Zhu[1,3], Qiuyu Xu[1,2], Yangkun Liu[1,2] and Hongshan Liu[1,2]

Abstract

In this study, the neutral wind observations from the Michelson Interferometer for Global High-resolution Thermospheric Imaging (MIGHTI) instrument onboard Ionospheric CONnections (ICON) are used to investigate the longitudinal structure of zonal wind between 100 and 300 km during daytime. The four-peaked structure in the longitudinal distribution between June and August is visually clear in the whole altitudinal range. The longitudinal wavenumber 1–4 patterns (WN1–WN4) are extracted, and the altitude–month distributions of WN1–WN4 and their contributions to the longitudinal structure are compared. The amplitudes of WN3 and WN4 show seasonal dependence, and the amplitude of WN4 exhibits obvious vertical propagation from the mesosphere and lower thermosphere (MLT) to the upper thermosphere in summer and autumn. WN1 is an important contributor to the longitudinal structure, WN4 is the primary contributor in the lower altitude ranges in summer and autumn at three latitudes. The contributions of WN3 (WN1) increase holistically with latitude in summer (spring, autumn, and winter). And the main wave sources of WN1–WN4 are further investigated in the 100–106 km and 210–300 km altitude regions. The main wave sources of WN1 and WN2 have complex variations with altitude, latitude, and season, while WN3 (WN4) is clearly influenced by DE2 (DE3 and SE2).

Keywords Thermospheric wind, Longitudinal structure, Altitudinal variation, Main wave sources

Graphical Abstract

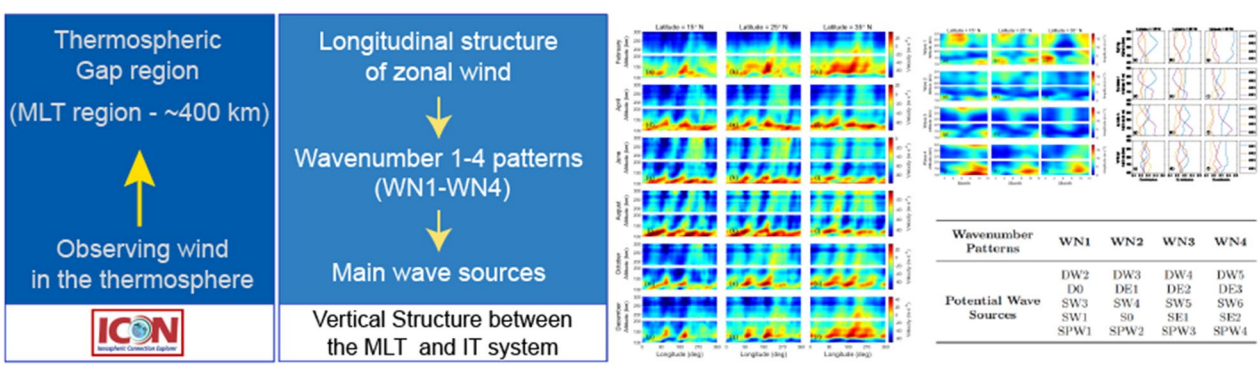

*Correspondence:
Hong Gao
hgao@spaceweather.ac.cn
Jiyao Xu
jyxu@spaceweather.ac.cn
Full list of author information is available at the end of the article

Introduction

The thermosphere is an important transition region between the Earth's atmosphere and space. Besides the influence of solar and geomagnetic activities, the thermosphere is also modulated by waves which generated from the lower atmosphere. The waves which are referred to as atmospheric "migrating" and "nonmigrating" tides with longer vertical wavelengths can propagate upward into the thermosphere, making thermospheric and ionospheric parameters exhibit global-scale variations (Forbes 1995; Oberheide and Gusev 2002; Immel et al. 2006). To date, plenty of studies have been devoted to the longitudinal structure of thermospheric and ionospheric parameters, such as airglow emission, temperature, wind, F-2 peak height, plasma density, total electron content, $\vec{E} \times \vec{B}$ drifts, nitric oxide (NO) density, and so on (e.g., Forbes et al. 1999; Fang et al. 2009; Liu et al. 2010; Pancheva and Mukhtarov 2010; Xu et al. 2010; Shepherd 2011; Ren et al. 2011; Gao et al. 2012; Ren et al. 2012). Investigating the longitudinal structure of thermospheric and ionospheric parameters helps us understand the effect of tides from the lower atmosphere to the thermosphere.

Among the atmospheric parameters, the wind is an important dynamical parameter in the thermosphere (Rishbeth 1967; Blanc and Richmond 1980; Richmond et al. 1992). As more observations and simulations become available, and the longitudinal structure of wind is better understood, more and more studies have been devoted to the investigation of wave sources of the longitudinal structure (e.g., Xiong et al. 2014; Truskowski et al. 2014; Jiang et al. 2018; Liu et al. 2021; Li et al. 2022). Investigating the main wave sources in a large altitude range helps understand the vertical coupling process between the lower atmosphere and the ionosphere–thermosphere (IT) system.

Based on the observation from the TIMED Doppler Interferometer (TIDI) onboard the Thermosphere Ionosphere Mesosphere Electrodynamics and Dynamics (TIMED) satellite, the longitudinal structures of wind in the MLT have been studied. The first climatological analysis of the diurnal and semidiurnal zonal and meridional wind tides from 85 to 105 km is displayed by using the data from TIDI (Akmaev et al. 2008; Oberheide et al. 2005, 2006, 2007, 2011b; Wu et al. 2008; Wan et al. 2010). The longitudinal structure of thermospheric wind and the important signals of nonmigrating tides at altitude ~ 400 km are studied based on the accelerometer onboard the CHAllenging Minisatellite Payload (CHAMP) satellite (Lühr et al. 2007; Häusler et al. 2007; Häusler and Lühr 2009; Häusler et al. 2010). The annual variation of the wave-4 structure of zonal wind and the tidal signatures at 400 km are also evaluated (e.g., Häusler and Lühr 2009; Xiong et al. 2015).

However, the "thermospheric gap" region locates between the MLT region and ~ 400 km (Oberheide et al. 2009, 2011a), which is proved to be an important region in the atmosphere with few wind observations. Oberheide et al. (2009, 2011b) have combined the observations from TIMED and CHAMP with the physics-based empirical fit model to analyze migrating and nonmigrating tides in the thermospheric gap region. However, investigating the thermospheric wind tides is difficult due to the limited global tidal observations. The Upper Atmosphere Research Satellite (UARS)/Wind Imaging Interferometer (WINDII) satellite provided neutral wind observation in the altitude range of 90–275 km. Cho and Shepherd (2012a) and Talaat and Lieberman (2010) have reported the four-peaked structure of zonal wind based on WINDII observations. However, the vertical variations and the main wave sources of the longitudinal structure of zonal wind still need to be further investigated in a large altitude range in the thermospheric gap region.

Fortunately, the Michelson Interferometer for Global High-resolution Thermospheric Imaging (MIGHTI) instrument onboard the Ionospheric Connection Explorer (ICON) mission can provide wind observation from 90 to 300 km during daytime, 90–106 km and 210–300 km during nighttime (Immel et al. 2017; Englert et al. 2017). Thus, the ICON/MIGHTI provides a new data source to investigate the vertical variations and the main wave sources of the longitudinal structure of zonal wind in the thermospheric gap region. In this study, by using the observation from ICON/MIGHTI, we are able to present the longitudinal structure of zonal wind from 100 km to 300 km altitude during daytime. The seasonal dependence of WN1–WN4 and their contribution to the longitudinal structure are studied, and the potential wave sources of WN1–WN4 are analyzed at 100–106 km and 210–300 km as ICON cannot provide wind observation between the two altitudinal ranges during nighttime (Englert et al. 2017; Immel et al. 2017).

This paper is organized as follows. The data and methods are given in "Data set and methods" section. The result and discussion about the longitudinal structure of zonal wind, the altitude–month distributions of WN1–WN4 and their contribution to the longitudinal structure are presented in "Results and discussion" section. And the analysis of the main wave sources of the longitude structure also is in "Results and discussion" section. The conclusions are given in the last section.

Data set and methods

The ICON mission, which launches on 11 October 2019, aims to observe neutral winds between 9° S and 42° N geographic latitude. It runs in an orbit with an inclination of about 27° at 575 km, and its orbital period is about 97 min. During the daytime, neutral wind profiles from 90 to 300 km are derived from two perpendicular tangent-point line-of-sight vector measurements. The neutral wind data in the altitude range of 90–210 km (180–300 km) are retrieved from the Doppler shift of the OI 557.7 nm green (OI 630.0 nm red) airglow emission line. During nighttime, the neutral wind data in the altitude range of 90–105 km are determined from the OI 557.7 nm green emission, while data in the altitude range of 210–300 km are determined from the OI 630.0 nm red airglow emission (Harding et al. 2017, 2021). The neutral winds are measured with an accuracy of 1.2-4.7 ms^{-1}, and the data have been validated against ground-based measurements (Harding et al. 2021; Makela et al. 2021).

In this study, we use the ICON/MIGHTI zonal wind V04 data with a quality factor of 1 from December 2019 to January 2022. During the daytime, the neutral wind data can cover the altitude range of 100–300 km by combining the winds of the red-line and green-line. There are no discontinuities in the overlapping areas, as the common zero-wind reference is used for the red-line and green-line (Harding et al. 2021; Makela et al. 2021). In this work, we present the longitudinal structure of zonal wind and the altitude–month distribution of WN1–WN4 during the daytime while the data between the 10:00–14:00 h LT are used. To ensure the accuracy of extracting the diurnal tides, the main wave sources of the longitudinal structure are analyzed below 106 km and above 210 km by using the full 24 h of LT data.

The data are processed as follows. Firstly, the observation data between 10° N and 40° N are separated into three latitudes: 10° N–20° N, 20° N–30° N, and 30° N –40° N, which are, respectively, referred to as 15° N, 25° N, and 35° N, here in after. Secondly, in each latitude bin, 51-day windows with the centers at the middle of each month are set. Previous studies indicate that ICON can provide data of nearly full 24-h local time coverage by using a 41-day window (Cullens et al. 2020, ?). In this study, the criterion for data selection is more rigorous and only the data with quality equal to 1 are used. Therefore, 51-day windows are used to make sure that there are enough data in the study of wave sources. Thirdly, corresponding to each month and latitude bin, the altitude profiles of zonal wind are binned in 36 30-degree windows in the longitude direction. The windows partially overlap and the centers of two adjacent windows are separated by 10° longitude. Averaging the profiles in the bins, we get the altitude profiles of zonal wind at 36 longitudes for each month and latitude bin. Then the altitude profiles are interpolated to 1 km in height. Fourthly, the longitudinal distributions of zonal wind at three latitudes for each month from 100 to 300 km are presented in Fig. 1. Finally, we fit the longitudinal structure of zonal wind with waves of zonal wavenumber 1–6 patterns (WN1–WN6, referred to as longitudinal wavenumber patterns) by using Eq. (1):

$$y^{\text{fit}} = A_0 + \sum_{n=1}^{6} A_n \cos\left[\frac{2\pi}{360} \cdot n \cdot (\lambda - \varphi_n)\right]. \quad (1)$$

Here λ denotes the longitude in degrees, A_0 denotes the zonal mean zonal wind, A_n and φ_n denote the amplitude and phase of the wavenumber n pattern, respectively. WN1–WN6 are extracted by fitting the longitudinal distribution of zonal wind with Eq. (1). The results indicate that WN5 and WN6 are very weak compared to WN1–WN4, so only the harmonics waves of WN1–WN4 are given in this paper.

Results and discussion

The longitudinal structure of zonal wind

Previous studies on the longitude structure of zonal wind in the thermospheric gap region have primarily relied on observations from the UARS spacecraft. Although these studies have improved our understanding of the longitudinal structures and the tides in this region, further research is still required. In this study, we provide a more detailed longitude structure of zonal wind and comprehensive analysis of longitudinal wave patterns over a wide altitude range. Figure 1 shows the altitude–longitude distribution of zonal wind from 100 to 300 km at three latitudes in 6 months. The altitude–longitude distribution in the overlap altitude region in both panels are generally consistent. This demonstrates that the ICON/MIGHTI zonal wind data from both the OI 630.0 nm red airglow emission line and OI 557.5 nm green airglow emission line can be combined to study the variations of the longitudinal structure with altitude.

The speed, direction, and altitude–longitude distribution of zonal wind vary with month and latitude. In general, westward zonal wind is predominant from 100 to 300 km in June and August at all latitudes (Fig. 1g–l), eastward and westward zonal wind predominates below and above 150 km in other months (Fig. 1a–f, m–r), respectively. The four-peaked structure is prominent in June and August (Fig. 1g–l) and lower altitudes in October (Fig. 1m–o). The WINDII observation also shows a similar four-peaked structure from 100 to 250 km in August (Cho and Shepherd 2012a).

Furthermore, the longitudes where the wave peaks appear gradually vary with altitude. Take Fig. 1j as an

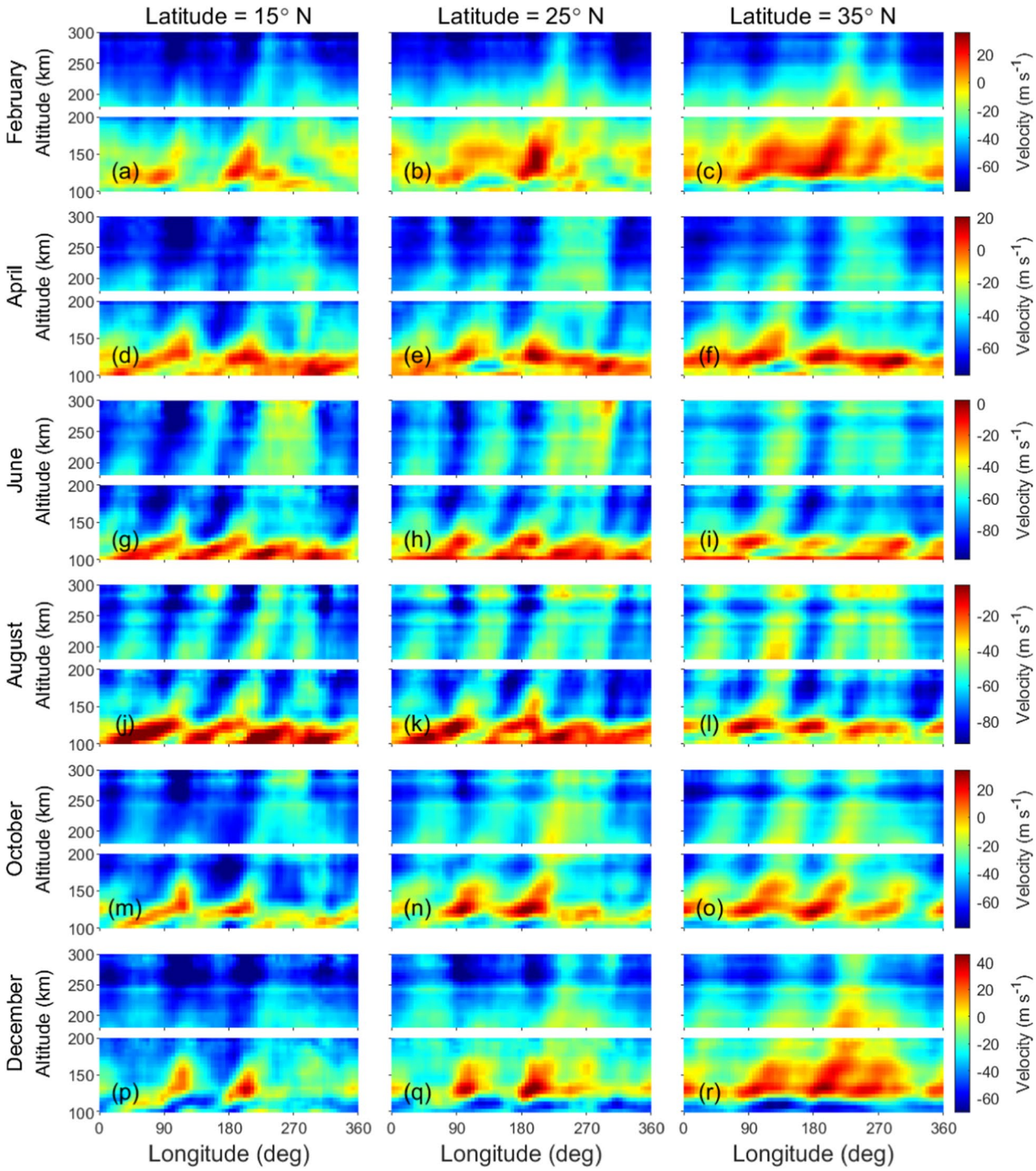

Fig. 1 The altitude–longitude distribution of zonal wind during daytime in the altitude range of 100–300 km at three latitudes, 15° N, 25° N, and 35° N. The local time is between 10:00 h and 14:00 h. Each subplot is divided into two panels, the top panel shows zonal wind from the 630.0 nm red line emission of atomic oxygen in the altitude range of 180–300 km, and the bottom panel shows zonal wind from the 557.7 nm green line emission of atomic oxygen in the altitude range of 100–210 km. **a**–**r** Represent the longitudinal structure of zonal wind in February, April, June, August, October and December at 15° N, 25° N and 35° N, respectively

example, the wave peaks appear at around 40°, 130°, 220° and 310° in longitude at 100 km, and gradually shift to 150°, 230°, 280° and 50° in longitude at 300 km. Such shift with altitude is generally faster below 150 km than that above 150 km, which is generally consistent with the early results of observation and simulation (e.g., Cho and Shepherd 2012a; England et al. 2010; Wu et al. 2012). The altitudinal variations of the phases of WN1–WN4 (not given here) derived from the fitting based on Eq. (1) are larger at lower altitudes than at higher altitudes, which may imply that the wave sources of the longitudinal structure at higher altitude have longer vertical wavelength than those at lower altitude. Oberheide et al. (2011b) pointed out that only the harder to dissipate long-wavelength mode propagates into the thermosphere, where amplitudes and phases finally relax to almost constant values as molecular diffusion becomes dominant.

Altitudinal and seasonal variations of WN1–WN4

As mentioned in the Data and methods section, the WN1–WN4 of the longitude structure are extracted by using Eq. (1) based on the observations within 10–14 LT. Figure 2 shows the altitude–month distribution of the amplitude of the WN1–WN4 at three latitudes. The altitude–month distribution of WN1 shows significant latitudinal dependence. At 15° N, the amplitude of WN1 shows two peaks occurring above 200 km from February to June and below 150 km from October to December,

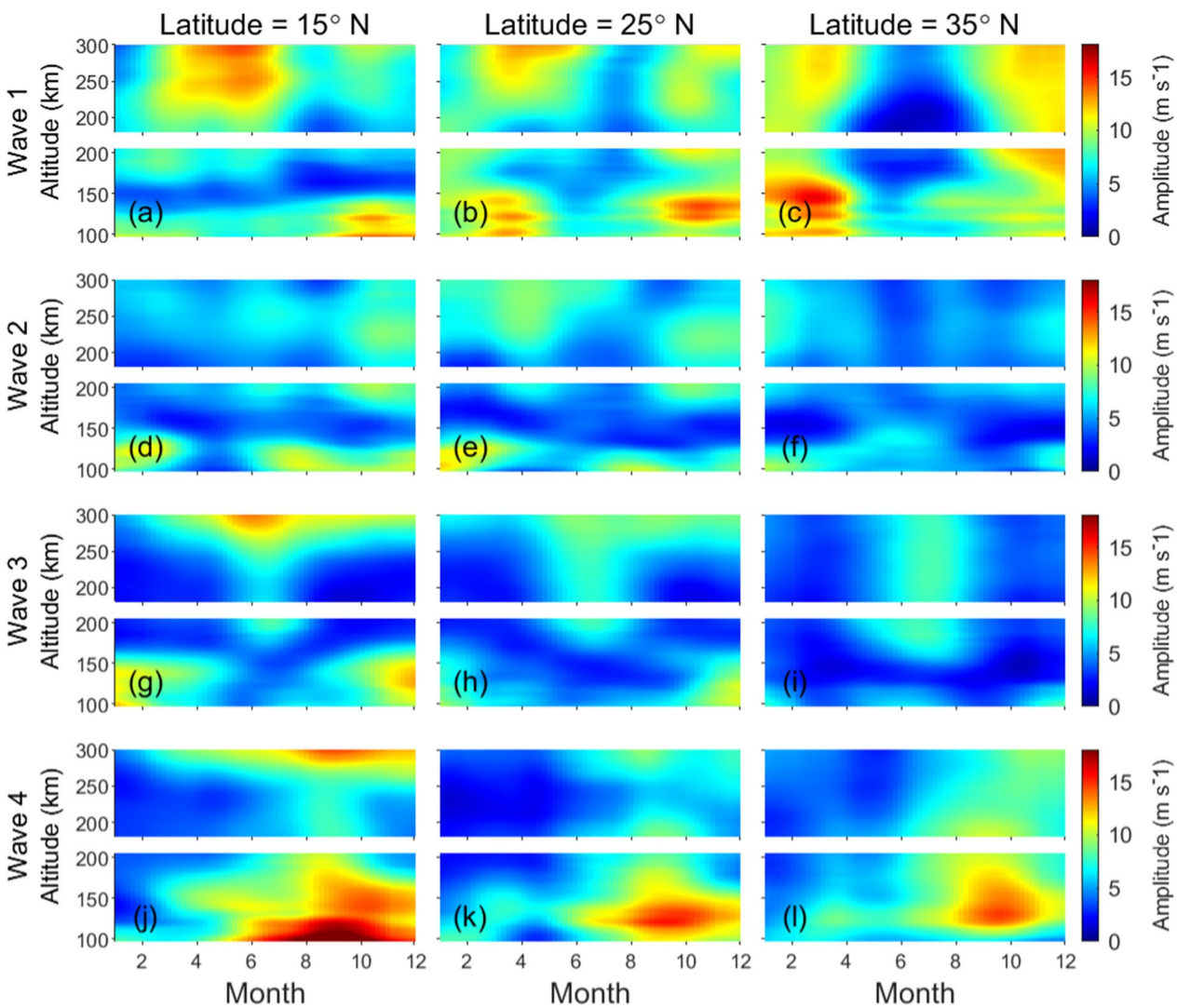

Fig. 2 The altitude–month distribution of amplitude of WN1–WN4 in the altitude range of 100–300 km at three latitudes (15° N, 25° N, and 35° N). The layout of each subplot is similar to Fig. 1. **a**–**l** Represent the altitude–month distribution of amplitude of WN1–WN4 at 15° N, 25° N and 35° N, respectively

respectively (Fig. 2a). At 25° N, as shown in Fig. 2b, the amplitude of WN1 is larger around April and October in the altitude range of 100–150 km and 200–300 km. At 35° N, the amplitude of WN1 is larger in spring and winter than those in other seasons in the whole altitude range (Fig. 2c). The amplitude of WN2 is in general small at ∼ 150 km at 15° N and 25° N (Fig. 2d, e), and so is the amplitude of WN1 at 15° N (Fig. 2a).

Several studies have shown that the longitudinal structure is caused by multiple tides (Häusler and Lühr 2009; Xiong et al. 2015; Jiang et al. 2018) and its potential tides vary with altitude (Akmaev et al. 2008; Hagan et al. 2009; Oberheide et al. 2009; Forbes et al. 2022). Thus, the smaller amplitude of WN1 and WN2 at ∼ 150 km can be attributed to the weak intensity of potential wave sources.

The amplitudes of WN3 and WN4 show vertical structure in altitude. For WN3, the peaks of amplitude appear in winter below 150 km and summer above 180 km at 15° N (Fig. 2g). With increasing latitude, the lower altitude region with a larger amplitude in winter gradually disappears, and the magnitude of maximum WN3 amplitude also gradually decreases from 13.4 m/s at 15° N to 8.1 m/s at 35° N ∼ 280 km. The amplitude of WN4 is larger in late summer and autumn than in other seasons, and it propagates vertically from the MLT to the upper atmosphere. The peaks of amplitude of WN4 also vary with latitude, situating ∼ 100 km at 15° N, ∼ 120 km at 25° N and 35° N. Similar to WN3, the magnitude of the maximum amplitude of WN4 also gradually decreases from 20.4 m/s at 15° N ∼ 100 km to 14.5 m/s at 35° N ∼ 120 km.

The seasonal variations of WN4 amplitude are similar to earlier studies which show that the four-peaked structure is most prominent in summer and autumn (Liu and Watanabe 2008). And the altitudinal and latitudinal variations of the amplitude of WN4 also are consistent with the variations of DE3 tide (Li et al. 2019). Earlier simulation indicates that DE3 tide is strong during summer and autumn at ∼ 100 km (Akmaev et al. 2008). As pointed out by Lieberman et al. (2013) and Oberheide et al. (2011b), DE3 tide also varies with altitude and decreases with latitude. In the following sections, the contributions of different potential wave sources to WN1–WN4 are further analyzed.

The contribution of WN1–WN4 to the longitudinal structure

To compare the individual contribution of WN1–WN4 to the longitudinal structures of zonal wind, the relative amplitude percentage (RAmp) is calculated from Eq. (2) during 10–14 LT at different altitudes, seasons, and latitudes. By using this method, Liu et al. (2021) has analyze the main wave sources contributions to the longitudinal structure of the equatorial electric field:

$$\mathrm{RAmp}_i = \frac{\overline{\mathrm{SAmp}_i}}{\sum_{\mathrm{i}=1}^{4} \overline{\mathrm{SAmp}_i}} \times 100\%. \tag{2}$$

$\overline{\mathrm{SAmp}_i}$ denotes the seasonal average amplitude of WN1–WN4, and the RAmp of WN1–WN4 in four seasons and three latitudes is shown from 100 to 300 km in Fig. 3.

In spring, WN2 and WN1 are the major contributors below and above 150 km at 15° N, respectively. The maximum contribution of WN1 is ∼ 230 km (> 40%) (Fig. 3a). The contribution of WN1 increases with latitude, WN1 becomes the primary contributor at 25° N and 35° N between 100–300 km (Fig. 3b, c). In summer, the major contributors are WN4 and WN1 at 15° N below and above 180 km, respectively. The maximum contribution of WN1 still appears ∼ 230 km (> 40%) (Fig. 3d). At 25° N, the major contributors are WN4 and WN1 below and above 150 km (Fig. 3e), respectively. While the contribution of WN3 increases with latitudes, WN4 and WN3 become the major contributor at 35° N below and above 180 km (Fig. 3f), respectively. In autumn, the contribution of WN4 is greater than in other seasons, and WN4 is the primary contributor from 100 to 300 km at 15° N and below 200 km at 25° N and 35° N (Fig. 3g–i). WN1 contributes most above 200 km at 25° N and 35° N. In winter, WN3 and WN2 are major contributors at 15° N below and above 170 km (Fig. 3j), respectively. WN1 becomes the primary contributor at 25° N and 35° N (Fig. 3k, l).

In summary, WN1 is a major contributor to the longitudinal structure of zonal wind for most altitudes, seasons and latitudes. Strong WN1 in the zonal wind was also reported by Xiong et al. (2015) based on the observations of CHAMP spacecraft at midlatitudes and this could be attributed to the nonmigrating tides of the zonal wind can be generated in situ through ion-neutral interactions in the upper atmosphere, which causes several tidal sources of WN1 (D0, DW2, SW1, and SW3) to be prominent (Xiong et al. 2015). Such a mechanism may also influence zonal wind between the MLT and upper thermosphere, indicating the need for further investigation and more attention to WN1 in future studies. Also, Jhuang et al. (2018) have studied the longitudinal structure of TEC and pointed out that WN2 is stronger than WN3 and WN4. This is not completely consistent with the result in this study. As shown in Fig. 3, at higher altitudes, the WN2 at 15° N and 25° N is indeed stronger than WN4 in four seasons except autumn; the WN2 at three latitudes is also, on the whole, stronger than WN3 except the higher altitudes in summer. However, at lower altitudes, the WN4

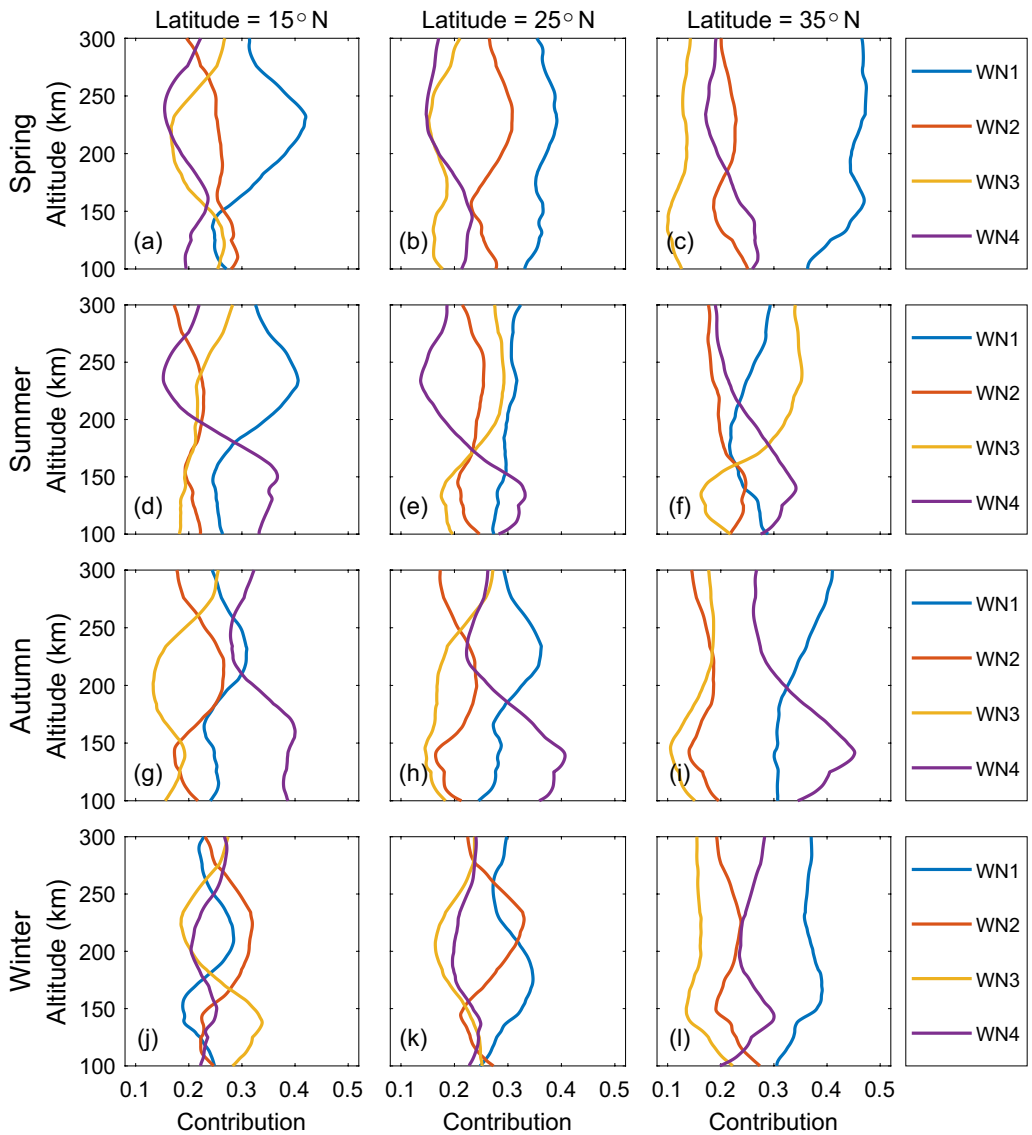

Fig. 3 The contribution of WN1–WN4 to the longitudinal structures in four seasons at three latitudes (15° N, 25° N, and 35° N) from 100 to 300 km. Blue, orange, yellow and purple lines represent WN1, WN2, WN3 and WN4, respectively. **a**–**m** Represent the contribution of WN1–WN4 to the longitudinal structure at 15° N, 25° N and 35° N in spring summer, autumn and winter, respectively

is stronger than WN2 in four seasons at 35° N and in summer and autumn at 15° N and 25° N. In addition, the contribution of the electron density in the F region in the ionosphere to the TEC is predominant. Therefore, the longitudinal structure of TEC given by Jhuang et al. (2018) is more consistent with that of the zonal wind at higher altitudes but different from that at lower altitudes as shown in Fig. 3. The contribution of WN1 increases with latitude in spring, autumn, and winter, and the contribution of WN3 increases with latitude in summer. In addition, the contribution of WN4 is greater below 200 km than above 200 km.

The main wave sources of WN1–WN4

WN1–WN4 are composed of different potential wave sources, which may vary with season, latitude and altitude. Therefore, the contribution of the tidal sources and stationary planetary waves to WN1–WN4 is calculated to analyze their influence on WN1–WN4. Note that here we only use the data in the altitude range of 100–106 km and 210–300 km due to the limitation of the data coverage.

Firstly, the wave potential sources of WN1–WN4 are identified based on previous studies. Five important tides and stationary waves for WN1–WN4 have been

Table 1 The potential sources of WN1–WN4

Wavenumber patterns	WN1	WN2	WN3	WN4
Potential wave sources	DW2	DW3	DW4	DW5
	D0	DE1	DE2	DE3
	SW3	SW4	SW5	SW6
	SW1	S0	SE1	SE2
	SPW1	SPW2	SPW3	SPW4

summarized (Häusler et al. 2007; Häusler and Lühr 2009), as listed in Table 1. Westward (W) and eastward (E) propagating diurnal tides (D), semidiurnal tides (S), and stationary planetary waves (SPW) are included.

Secondly, we extract the WN1–WN4 components at each LT between 1 LT to 24 LT by using Eq. (1). Then in the LT frame, WN1–WN4 [(the left-hand side of Eq. (3)] are fitted with their potential wave sources (are listed in Table 1) by using the following Eq. (3) (Liu et al. 2021):

$$A_n \cos\left[\frac{2\pi}{360}\cdot n\cdot(\lambda-\varphi_n)\right] = \sum a_i \cos\left[\sigma_i\cdot\frac{2\pi}{24}\cdot t_{\mathrm{LT}} + \frac{2\pi}{360}\cdot(s_i-\sigma_i)\cdot\lambda+\phi_i\right]. \tag{3}$$

The potential wave sources are superimposed on the right-hand side of Eq. (3). $\sigma_i = 0$, 1, and 2, representing stationary planetary waves, diurnal tides and semidiurnal tides, respectively. s_i denotes the wavenumber of the ith potential wave sources in the universal time (UT) frame (W: positive; E: negative; standing: 0). In addition, $|s_i - \sigma_i| = n$, which represents the wavenumber of the ith potential sources in the LT frame. In Eq. (3), a_i and ϕ_i denote the amplitude and phase of the ith potential sources, respectively. The t_{LT} represents LT in hours. The fitting procedure is performed corresponding to all longitudes during 24 LT by using the non-linear least squares method. And this fitting is performed for each latitude, altitude and month.

Thirdly, the potential sources listed in Table 1 are validated by Eq. (3). WN1–WN4 are reconstructed from corresponding potential sources. Figure S1 in Additional file 1 shows the reconstructed results of WN1–WN4 in January at 106 km and 250 km (other reconstructed results are not shown in this study). The reconstructed amplitudes and phases are in good agreement with the amplitudes and phases of original wavenumber patterns, proving the validity of the potential sources selected in the first step.

Finally, the contribution of potential sources (CPS) to WN1–WN4 in the four seasons are calculated from Eq. (4):

$$\mathrm{CPS}_{ni} = \frac{a_i}{\sum a_i}\times 100\%(i=1,2,3,4,5). \tag{4}$$

The observational data from the UARS spacecraft were ever used to study several certain wave sources of certain longitudinal wavenumber patterns of zonal wind in the thermospheric gap region (e.g., Lieberman et al. 2013; Cho and Shepherd 2015). In this study, we present a comprehensive quantitative analysis of the primary wave sources of WN1–WN4 at various altitudes during different seasons. Figure 4 shows the contribution of potential wave sources to WN1. At the 100–106 km altitudes (lower altitude range), at 15° N, the primary contributor is SPW1 in spring and autumn, and DW2 contribute the most in summer and winter. At 25° N, D0 is the primary contributor in spring and summer, and DW2 becomes the primary contributor in autumn and winter. At 35° N, the main contributors are DW2 and SW1 in spring and winter, respectively. And in summer and autumn, it is SW3. At the 210–300 km altitudes (upper altitude range), in spring, the main contributor is SW3 at 15° N, and D0 is the main contributor at 25° N and 35° N. In summer, SPW1 is the main contributor at 15° N and 25° N, and D0 and SW3 contribute the most at 35° N. In autumn and winter, D0 is the main contributor.

Figure 5 shows the contribution of potential sources to WN2. We focus on spring at 15° N and on winter at 15° N and 25° N, when WN2 is the prominent contributor to the longitudinal structure. SW4 is the primary contributor at the lower altitude range in spring and winter at three latitudes. In winter at the upper altitude range, SW4 and DE1 are the primary contributors at 15° N and 25° N, respectively.

The contribution of potential sources to WN3 is shown in Fig. 6. For WN3, DE2 is mainly the most important contributor, whose contribution can even exceed 60% (Fig. 6a, d and j).

As for WN4, DE3 and SE2 are the primary contributors (Fig. 7). At the upper altitude range, the contribution of SE2 tide is usually much larger than that of other tides except for Summer and Autumn at 15° N and 25° N, where DE3 contributes the most. At the lower altitude range, the contribution of DE3 is usually the largest except for Spring to Autumn at 35° N, where SE2 contributes the most. However, this result about SE2 is different from previous simulations based

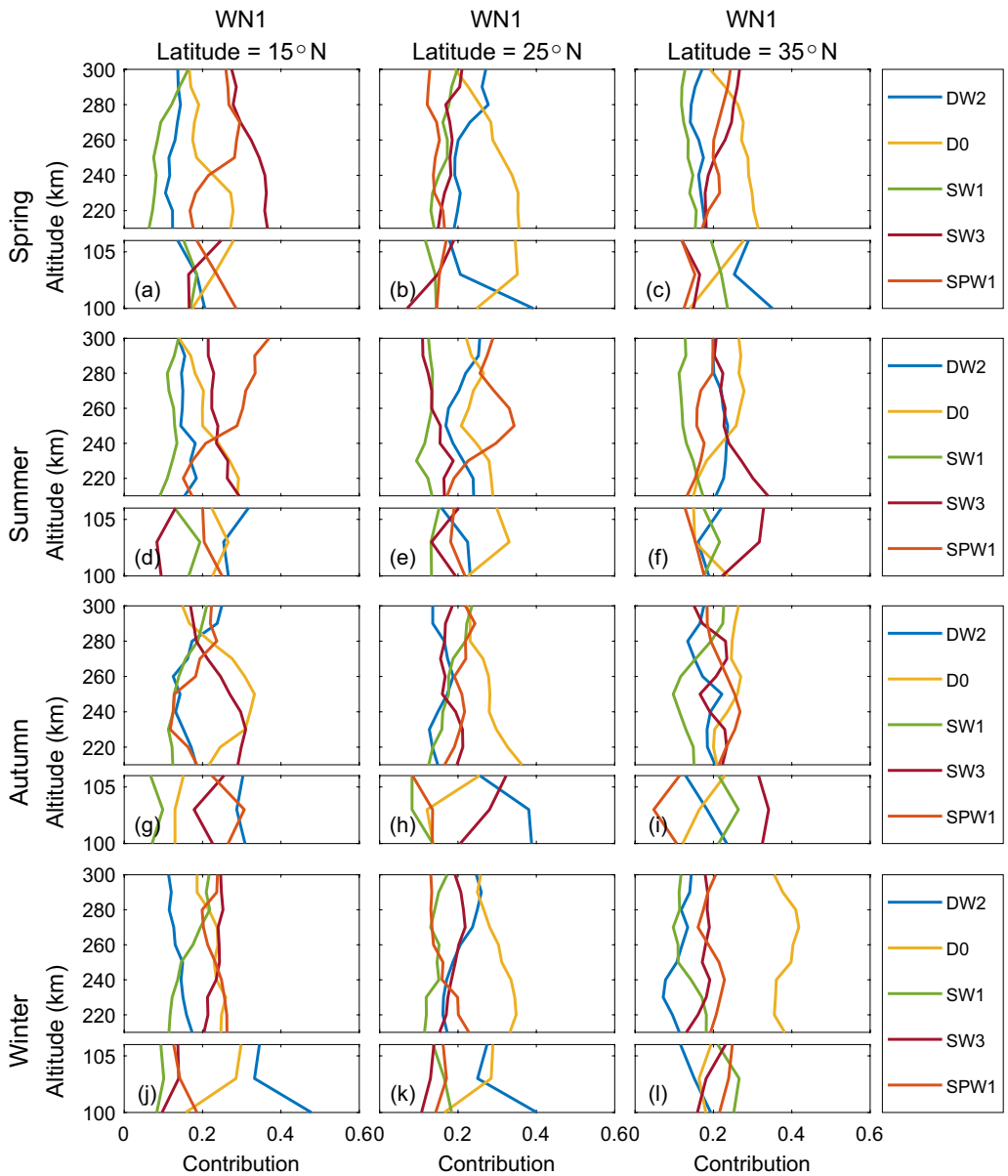

Fig. 4 The contribution of potential sources to WN1 in the altitude range of 100–106 km and 210–300 km in four seasons at three latitudes. Each subplot is divided into two panels, the top and bottom panels cover the altitude range of 210–300 km and 100–106 km, respectively. The blue, green, yellow, purple and orange line indicate the contribution of DW2, D0, SW1, SW3 and SPW1, respectively

on $\vec{E} \times \vec{B}$ drift velocity and ionospheric peak density (NmF2), which suggests that SE2 is not a contributor to WN4 (Pedatella et al. 2012). This may be due to the influence of SE2 being different between zonal wind and $\vec{E} \times \vec{B}$ drift velocity and ionospheric peak density. Further comparison and analysis are needed in future studies.

Conclusions

The neutral wind observations from ICON/MIGHTI provide a new insight to study the longitudinal structure of zonal wind and the altitude–month distribution of WN1–WN4 in the "thermospheric gap" region. And they are important data source to analyze the main wave sources of WN1–WN4 to the longitudinal structure in a larger altitude range.

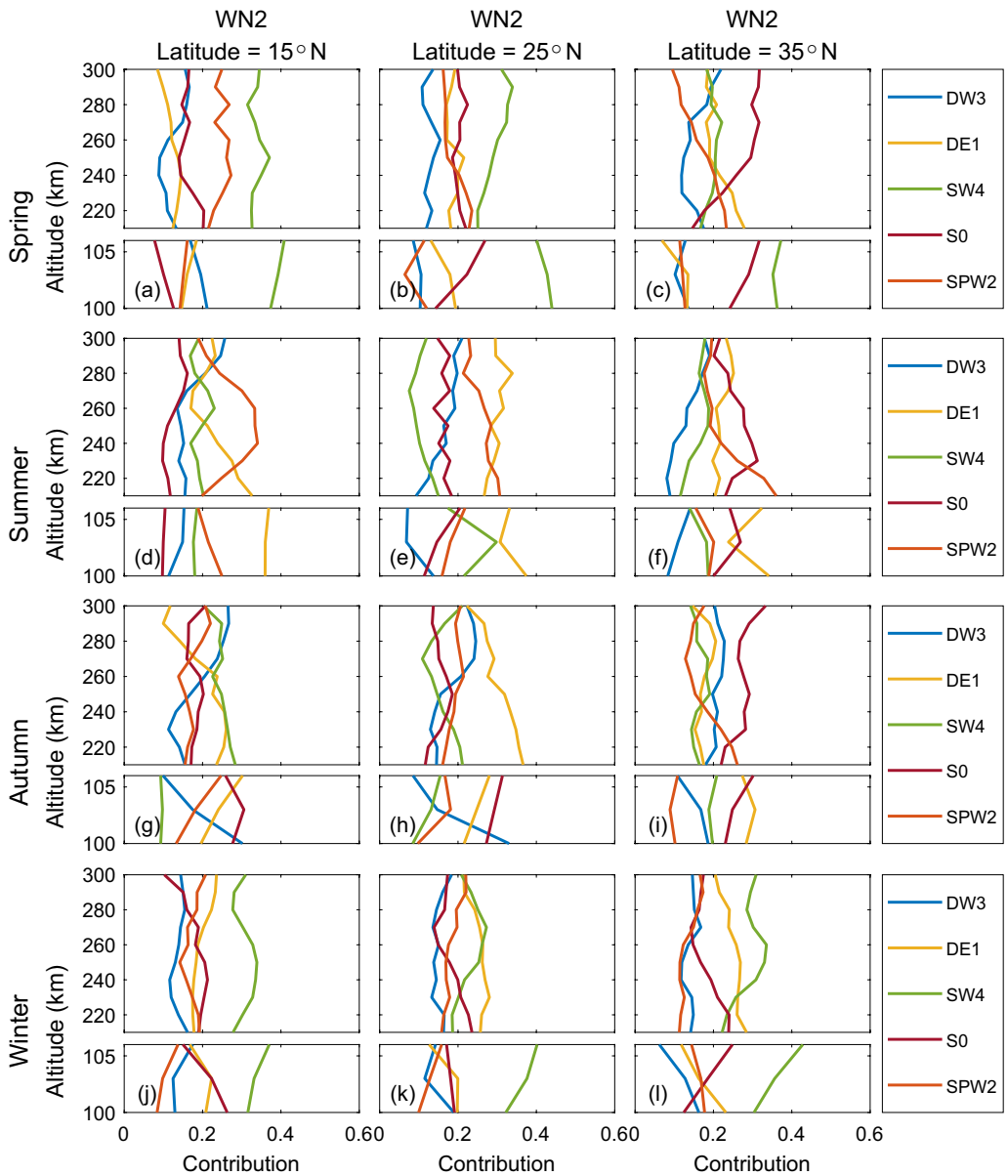

Fig. 5 Same as Fig. 4, but shows the contribution of potential sources to WN2, the blue, yellow, green, purple and orange line represent DW3, DE1, SW4, S0 and SPW2, respectively

In this study, we present the longitudinal structure of zonal wind and extract the amplitudes and phases of WN1–WN4 from 100 to 300 km in different months at low-middle latitudes, and then compare the altitude–month distribution of the amplitude of WN1–WN4. In addition, the main wave sources of WN1–WN4 are further analyzed in different seasons, latitudes and altitudes. The main conclusions can be summarized as follows:

1. The longitudinal structure of zonal wind varies with month and latitude from 100 to 300 km, the four-peaked structure is prominent between June and August and lower altitudes in October.
2. The altitude–month distributions of WN1 have significant latitudinal dependence. At 15° N, the amplitude of WN1 ~ 150 km is small in all seasons. At 25° N and 35° N, the amplitude of WN1 is small around summer from 100 to 300 km.
3. WN3 and WN4 have significant seasonal dependence in the altitude range of 100–300 km. The amplitude of WN3 is enhanced in winter below 150 km and in summer above 200 km. The WN4 amplitude

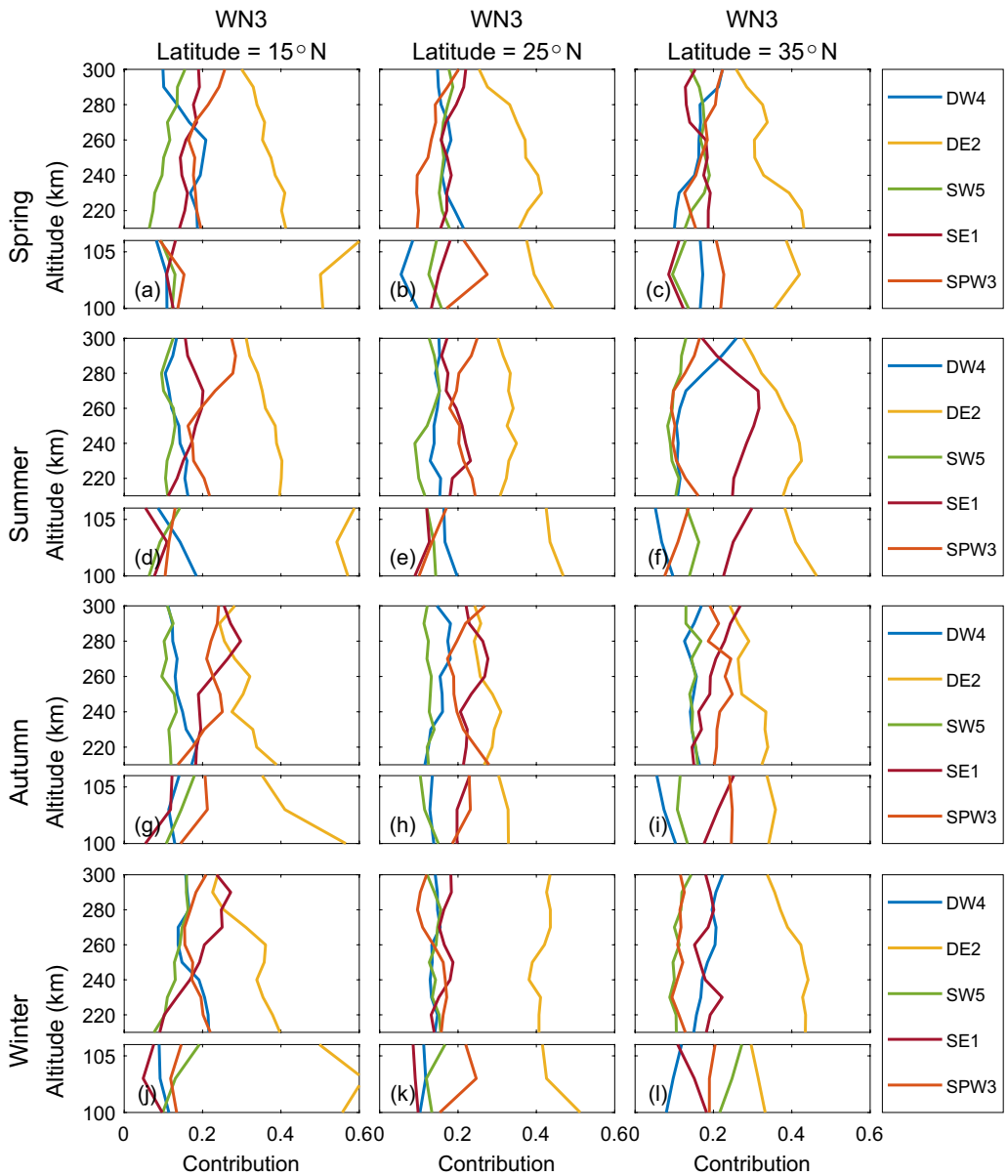

Fig. 6 Same as Fig. 4, but shows the contribution of potential sources to WN3, the blue, yellow, green, purple and orange line represent DW4, DE2, SW5, SE1 and SPW3, respectively

is enhanced in late summer and autumn between 100 and 300 km, with peaks appearing in the MLT region. And the amplitude of WN4 shows a vertical propagation from the MLT to the upper thermosphere.

4. WN1 has a significant contribution to the longitudinal structure in four seasons. Especially at 35° N, the contribution of WN1 is larger than 45% in spring and is about 40% in winter, respectively (Fig. 3c, i). WN4 remains the primary contributor in the summer and autumn at the lower altitude range (Fig. 3d–i), especially it contributes more than 40% to the longitudinal structure in autumn (Fig. 3g–i). The contribution of WN1 to the longitudinal structure increases holistically with latitudes in spring, autumn and winter, and the contribution of WN3 to the longitudinal structure also increases holistically with latitude in summer.
5. The main wave sources of WN1 and WN2 have complex variations. The contribution of DE2 to WN3 is quite prominent (Fig. 6a–l). DE3 and SE2 are the

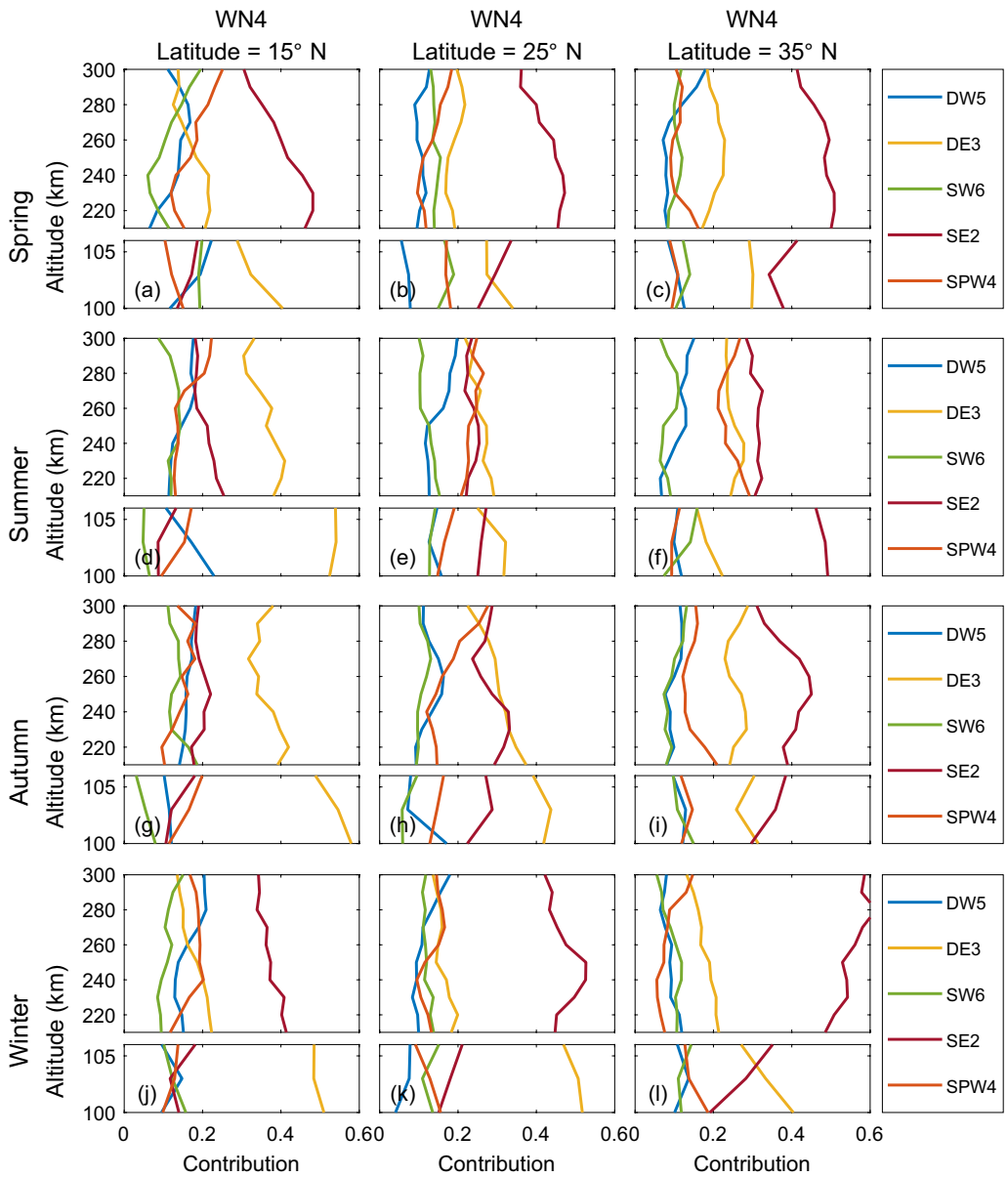

Fig. 7 Same as Fig. 4, but shows the contribution of potential sources to WN2, the blue, yellow, green, purple and orange line represent DW5, DE3, SW6, SE2 and SPW4, respectively

major contributors to WN4, and the contribution of SE2 increases with increasing latitude.

Abbreviations

ICON	Ionospheric CONnections
MIGHTI	Michelson Interferometer for Global High-resolution Thermospheric Imaging
TIMED	Thermosphere Ionosphere Mesosphere Electrodynamics and Dynamics
TIDI	TIMED Doppler Interferometer
CHAMP	CHAllenging Minisatellite Payload
UARS	Upper Atmosphere Research Satellite
WINDII	Wind Imaging Interferometer
WN1–WN6	Wavenumber 1–6 patterns
LT	Local time
UT	Universal time
MLT	Mesosphere and lower thermosphere
NO	Nitric oxide
IT	Ionosphere–thermosphere
RAmp	Relative amplitude percentage
W	Westward
E	Eastward
D	Diurnal
S	Semidiurnal

SPW Stationary planetary waves
CPS Contribution of potential sources

Supplementary Information

The online version contains supplementary material available at https://doi.org/10.1186/s40623-023-01813-8.

Additional file 1. The original and reconstructed local time-longitude distributions for WN1-WN4 at 106 km and 250 km at 35°N in January. The top and bottom panels in each subplot indicate the original and reconstructed results, respectively.

Acknowledgements
The authors would like to thank the ICON mission team for their efforts to provide the data used in this study. The authors also thank Igor Koltovskoi for his constructive comments during the revision process.

Author contributions
DL performed the data analysis and wrote the manuscript; HG and YZ contributed to the conception and supervised the study; JX is involved with acquisition of funding and administration of the project; QX contributed to data analysis, code and manuscript preparation; YL and HL helped perform the analysis with constructive discussions. All authors read and approved the final manuscript.

Funding
This work is supported by the National Science Foundation of China (41774160 and 41831073). This work is also supported by the Pandeng Program of the National Space Science Center, Chinese Academy of Sciences, the Youth Cross Team Scientific Research Project of the Chinese Academy of Sciences (JCTD-2021-10), China–Russia Joint Research Program on Middle and Upper Atmosphere and Ionosphere, and Hainan National Field Science Observation and Research Observatory for Space Weather.

Availability of data and materials
The datasets generated and/or analyzed during the current study are available on the ICON Science Operations Center (https://icon.ssl.berkeley.edu/Data).

Declarations

Competing interests
The authors acknowledge that there are no conflicts of interest.

Author details
[1]Key Laboratory of Solar Activity and Space Weather, National Space Science Center, Chinese Academy of Sciences, Zhongguancun Street, Beijing 100190, China. [2]School of Earth Science, University of Chinese Academy of Sciences, Jingjia Road, Beijing 101408, China. [3]School of Astronomy and Space Science, University of Chinese Academy of Sciences, Jingjia Road, Beijing 101408, China.

Received: 27 December 2022 Accepted: 30 March 2023
Published online: 23 April 2023

References

Akmaev RA, Fuller-Rowell TJ, Wu F, Forbes JM, Zhang X, Anghel AF, Iredell MD, Moorthi S, Juang HM (2008) Tidal variability in the lower thermosphere: comparison of Whole Atmosphere Model (WAM) simulations with observations from TIMED. Geophys Res Lett. https://doi.org/10.1029/2007GL032584

Blanc M, Richmond A (1980) The ionospheric disturbance dynamo. J Geophys Res Space Phys 85(A4):1669–1686. https://doi.org/10.1029/JA085iA04p01669

Cho YM, Shepherd GG (2012) Propagation in longitude and altitude of wave 4 thermospheric perturbations from WINDII data at low and high latitudes. J Geophys Res Space Phys. https://doi.org/10.1029/2012JA018110

Cho YM, Shepherd G (2015) Resolving daily wave 4 nonmigrating tidal winds at equatorial and midlatitudes with WINDII: DE3 and SE2. J Geophys Res Space Phys 120(11):10053–10068. https://doi.org/10.1002/2015JA021903

Cullens CY, Immel TJ, Triplett CC, Wu YJ, England SL, Forbes JM, Liu G (2020) Sensitivity study for ICON tidal analysis. Progr Earth Planet Sci 7(1):1–13. https://doi.org/10.1186/s40645-020-00330-6

England SL, Immel TJ, Huba JD, Hagan ME, Maute A, DeMajistre R (2010) Modeling of multiple effects of atmospheric tides on the ionosphere: an examination of possible coupling mechanisms responsible for the longitudinal structure of the equatorial ionosphere. J Geophys Res Space Phys. https://doi.org/10.1029/2009JA014894

Englert CR, Harlander JM, Brown CM, Marr KD, Miller IJ, Stump JE, Hancock J, Peterson JQ, Kumler J, Morrow WH, Mooney TA, Ellis S, Mende SB, Harris SE, Stevens MH, Makela JJ, Harding BJ, Immel TJ (2017) Michelson interferometer for global high-resolution thermospheric imaging (MIGHTI): instrument design and calibration. Space Sci Rev 212(1):553–584. https://doi.org/10.1007/s11214-017-0358-4

Fang TW, Kil H, Millward G, Richmond AD, Liu JY, Oh SJ (2009) Causal link of the wave-4 structures in plasma density and vertical plasma drift in the low-latitude ionosphere. J Geophys Res Space Phys. https://doi.org/10.1029/2009JA014460

Forbes JM (1995) Tidal and planetary waves. The upper mesosphere and lower thermosphere: a review of experiment and theory. American Geophysical Union (AGU), Washington, DC, pp 67–87. https://doi.org/10.1029/GM087p0067

Forbes JM, Palo SE, Marcos FA (1999) Longitudinal structures in lower thermosphere density. J Geophys Res Space Phys 104(A3):4373–4385. https://doi.org/10.1029/1998JA900036

Forbes JM, Oberheide J, Zhang X, Cullens C, Englert CR, Harding BJ, Harlander JM, Marr KD, Makela JJ, Immel TJ (2022) Vertical coupling by solar semi-diurnal tides in the thermosphere from ICON/MIGHTI measurements. J Geophys Res Space Phys 127(5):e2022JA030,288. https://doi.org/10.1029/2022JA030288

Gao H, Nee J, Chen G (2012) Longitudinal distribution of O2 nightglow brightness observed by TIEMD/SABER satellite. Sci China Technol Sci 55(5):1258–1263. https://doi.org/10.1007/s11431-012-4802-0

Hagan ME, Maute A, Roble RG (2009) Tropospheric tidal effects on the middle and upper atmosphere. J Geophys Res Space Phys. https://doi.org/10.1029/2008JA013637

Harding BJ, Makela JJ, Englert CR, Marr KD, Harlander JM, England SL, Immel TJ (2017) The MIGHTI wind retrieval algorithm: description and verification. Space Sci Rev 212(1):585–600. https://doi.org/10.1007/s11214-017-0359-3

Harding BJ, Chau JL, He M, Englert CR, Harlander JM, Marr KD, Makela JJ, Clahsen M, Li G, Ratnam MV, Bhaskar Rao SV, Wu YJJ, England SL, Immel TJ (2021) Validation of ICON-MIGHTI thermospheric wind observations: 2. Green-line comparisons to specular meteor radars. J Geophys Res Space Phys 126(3):e2020JA028,947. https://doi.org/10.1029/2020JA028947

Häusler K, Lühr H (2009) Nonmigrating tidal signals in the upper thermospheric zonal wind at equatorial latitudes as observed by CHAMP. Ann Geophys 27(7):2643–2652. https://doi.org/10.5194/angeo-27-2643-2009

Häusler K, Lühr H, Rentz S, Köhler W (2007) A statistical analysis of longitudinal dependences of upper thermospheric zonal winds at dip equator latitudes derived from CHAMP. J Atmos Sol-Terr Phys 69(12):1419–1430. https://doi.org/10.1016/j.jastp.2007.04.004

Häusler K, Lühr H, Hagan ME, Maute A, Roble RG (2010) Comparison of CHAMP and TIME-GCM nonmigrating tidal signals in the thermospheric zonal wind. J Geophys Res Atmos. https://doi.org/10.1029/2009JD012394

Immel TJ, Sagawa E, England SL, Henderson SB, Hagan ME, Mende SB, Frey HU, Swenson CM, Paxton LJ (2006) Control of equatorial ionospheric morphology by atmospheric tides. Geophys Res Lett. https://doi.org/10.1029/2006GL026161

Immel TJ, England SL, Mende SB, Heelis RA, Englert CR, Edelstein J, Frey HU, Korpela EJ, Taylor ER, Craig WW, Harris SE, Bester M, Bust GS, Crowley G, Forbes JM, Gérard JC, Harlander JM, Huba JD, Hubert B, Kamalabadi F, Makela JJ, Maute AI, Meier RR, Raftery C, Rochus P, Siegmund OHW, Stephan AW, Swenson GR, Frey S, Hysell DL, Saito A, Rider KA, Sirk MM (2017) The ionospheric connection explorer mission: mission goals and design. Space Sci Rev 214(1):13. https://doi.org/10.1007/s11214-017-0449-2

Jhuang HK, Tsai TC, Lee LC, Ho YY (2018) Ionospheric tidal waves observed from global ionosphere maps: analysis of total electron content. J Geophys Res Space Phys 123(8):6776–6797. https://doi.org/10.1029/2018JA025242
Jiang J, Wan W, Ren Z, Yue X (2018) Asymmetric DE3 causes WN3 in the ionosphere. J Atmos Sol-Terr Phys 173:14–22. https://doi.org/10.1016/j.jastp.2018.04.006
Li X, Wan W, Cao J, Ren Z (2019) Meteorological scale correlation relationship of the ionospheric longitudinal structure wavenumber 4 and upper atmospheric daily DE3 tide. J Geophys Res Space Phys 124(3):2046–2057. https://doi.org/10.1029/2018JA026253
Li X, Ren Z, Cao J, Yu Y, Wang Y, Zhou X (2022) Comparative study of the variability of the non-migrating tide DE3 using WACCM-X simulations and TIMED/SABER observations. Earth Space Sci 9(2):e2021EA002,117. https://doi.org/10.1029/2021EA002117
Lieberman RS, Akmaev RA, Fuller-Rowell TJ, Doornbos E (2013) Thermospheric zonal mean winds and tides revealed by CHAMP. Geophys Res Lett 40(10):2439–2443. https://doi.org/10.1002/grl.50481
Liu G, Immel TJ, England SL, Kumar KK, Ramkumar G (2010) Temporal modulations of the longitudinal structure in F2 peak height in the equatorial ionosphere as observed by COSMIC. J Geophys Res Space Phys. https://doi.org/10.1029/2009JA014829
Liu H, Watanabe S (2008) Seasonal variation of the longitudinal structure of the equatorial ionosphere: does it reflect tidal influences from below? J Geophys Res Space Phys. https://doi.org/10.1029/2008JA013027
Liu Y, Xu J, Xiong C, Liu X, Guo B (2021) Main wave sources of the longitudinal structures of equatorial electric field. Geophys Res Lett 48(9):e2021GL092,426. https://doi.org/10.1029/2021GL092426
Lühr H, Häusler K, Stolle C (2007) Longitudinal variation of F region electron density and thermospheric zonal wind caused by atmospheric tides. Geophys Res Lett. https://doi.org/10.1029/2007GL030639
Makela JJ, Baughman M, Navarro LA, Harding BJ, Englert Christoph R, Harlander JM, Marr KD, Benkhaldoun Z, Kaab M, Immel TJ (2021) Validation of ICON-MIGHTI thermospheric wind observations: 1. Nighttime red-line ground-based fabry-perot interferometers. J Geophys Res Space Phys 126(2):e2020JA028,726. https://doi.org/10.1029/2020JA028726
Oberheide J, Gusev OA (2002) Observation of migrating and nonmigrating diurnal tides in the equatorial lower thermosphere. Geophys Res Lett 29(24):20-1–20-4. https://doi.org/10.1029/2002GL016213
Oberheide J, Wu Q, Ortland DA, Killeen TL, Hagan ME, Roble RG, Niciejewski RJ, Skinner WR (2005) Non-migrating diurnal tides as measured by the TIMED Doppler interferometer: preliminary results. Adv Space Res 35(11):1911–1917. https://doi.org/10.1016/j.asr.2005.01.063
Oberheide J, Wu Q, Killeen TL, Hagan ME, Roble RG (2006) Diurnal nonmigrating tides from TIMED Doppler Interferometer wind data: monthly climatologies and seasonal variations. J Geophys Res Space Phys. https://doi.org/10.1029/2005JA011491
Oberheide J, Wu Q, Killeen TL, Hagan ME, Roble RG (2007) A climatology of nonmigrating semidiurnal tides from TIMED Doppler Interferometer (TIDI) wind data. J Atmos Sol-Terr Phys 69(17):2203–2218. https://doi.org/10.1016/j.jastp.2007.05.010
Oberheide J, Forbes JM, Häusler K, Wu Q, Bruinsma SL (2009) Tropospheric tides from 80 to 400 km: propagation, interannual variability, and solar cycle effects. J Geophys Res Atmos. https://doi.org/10.1029/2009JD012388
Oberheide J, Forbes JM, Zhang X, Bruinsma SL (2011) Climatology of upward propagating diurnal and semidiurnal tides in the thermosphere. J Geophys Res Space Phys. https://doi.org/10.1029/2011JA016784
Oberheide J, Forbes JM, Zhang X, Bruinsma SL (2011) Wave-driven variability in the ionosphere-thermosphere-mesosphere system from TIMED observations: what contributes to the "wave 4"? J Geophys Res Space Phys. https://doi.org/10.1029/2010JA015911
Pancheva D, Mukhtarov P (2010) Strong evidence for the tidal control on the longitudinal structure of the ionospheric F-region. Geophys Res Lett. https://doi.org/10.1029/2010GL044039
Pedatella NM, Hagan ME, Maute A (2012) The comparative importance of DE3, SE2, and SPW4 on the generation of wavenumber-4 longitude structures in the low-latitude ionosphere during September equinox. Geophys Res Lett. https://doi.org/10.1029/2012GL053643
Ren Z, Wan W, Liu L, Xiong J (2011) Simulated longitudinal variations in the lower thermospheric nitric oxide induced by nonmigrating tides. J Geophys Res Space Phys. https://doi.org/10.1029/2010JA016131
Ren Z, Wan W, Liu L, Xiong J (2012) Simulated longitudinal variations in the E-region plasma density induced by non-migrating tides. J Atmos Sol-Terr Phys 90–91:68–76. https://doi.org/10.1016/j.jastp.2011.12.004
Richmond AD, Ridley EC, Roble RG (1992) A thermosphere/ionosphere general circulation model with coupled electrodynamics. Geophys Res Lett 19(6):601–604. https://doi.org/10.1029/92GL00401
Rishbeth H (1967) The effect of winds on the ionospheric F2-peak. J Atmos Terr Phys 29(3):225–238. https://doi.org/10.1016/0021-9169(67)90192-4
Shepherd GG (2011) Thermospheric observations of equatorial wavenumber 4 density perturbations from WINDII data. Geophys Res Lett. https://doi.org/10.1029/2011GL046986
Talaat ER, Lieberman RS (2010) Direct observations of nonmigrating diurnal tides in the equatorial thermosphere. Geophys Res Lett. https://doi.org/10.1029/2009GL041845
Truskowski AO, Forbes JM, Zhang X, Palo SE (2014) New perspectives on thermosphere tides: 1. Lower thermosphere spectra and seasonal-latitudinal structures. Earth Planets Space 66(1):136. https://doi.org/10.1186/s40623-014-0136-4
Wan W, Xiong J, Ren Z, Liu L, Zhang ML, Ding F, Ning B, Zhao B, Yue X (2010) Correlation between the ionospheric WN4 signature and the upper atmospheric DE3 tide. J Geophys Res Space Phys. https://doi.org/10.1029/2010JA015527
Wu Q, McEwen D, Guo W, Niciejewski RJ, Roble RG, Won YI (2008) Long-term thermospheric neutral wind observations over the northern polar cap. J Atmos Sol-Terr Phys 70(16):2014–2030. https://doi.org/10.1016/j.jastp.2008.09.004
Wu Q, Ortland DA, Foster B, Roble RG (2012) Simulation of nonmigrating tide influences on the thermosphere and ionosphere with a TIMED data driven TIEGCM. J Atmos Sol-Terr Phys 90–91:61–67. https://doi.org/10.1016/j.jastp.2012.02.009
Xiong C, Lühr H, Stolle C (2014) Seasonal and latitudinal variations of the electron density nonmigrating tidal spectrum in the topside ionospheric F region as resolved from CHAMP observations. J Geophys Res Space Phys 119(12):10416–10425. https://doi.org/10.1002/2014JA020354
Xiong C, Zhou YL, Lühr H, Ma SY (2015) Tidal signatures of the thermospheric mass density and zonal wind at midlatitude: CHAMP and GRACE observations. Ann Geophys 33(2):185–196. https://doi.org/10.5194/angeo-33-185-2015
Xu J, Smith AK, Jiang G, Gao H, Wei Y, Mlynczak MG, Russell JM III (2010) Strong longitudinal variations in the OH nightglow. Geophys Res Lett. https://doi.org/10.1029/2010GL043972

Publisher's Note